Molecular Insights into the Rescue Mechanism of an hERG Activator Against Severe LQT2 Mutations

Amit Kumawat[1,†,‡], Elisa Tavazzani[2,3,‡], Giovanni Lentini[4], Alessandro Trancuccio[2,3], Deni Kukavica[2,3], Marco Denegri[2], Silvia G. Priori[2,3,5,*], and Carlo Camilloni[1,*]

[1] Department of Biosciences, University of Milan, Milan, Italy
[2] IRCCS Istituti Clinici Scientifici Maugeri, Pavia, Italy
[3] Molecular Cardiology, Department of Molecular Medicine, University of Pavia, Pavia, Italy
[4] Department of Pharmacy-Pharmaceutical Sciences, University of Bari Aldo Moro, Bari, Italy
[5] Centro Nacional de Investigaciones Cardiovasculares Carlos III, Madrid, Spain

Corresponding Author
* Silvia G. Priori: silvia.priori@icsmaugeri.it and Carlo Camilloni: carlo.camilloni@unimi.it

Present Addresses
† Amit Kumawat: Department of Physics, University of Cagliari, Cagliari, Italy.

Abstract

Mutations in the hERG potassium channel are a major cause of long QT syndrome type 2 (LQT2), which can lead to sudden cardiac death. The hERG channel plays a critical role in the repolarization of the myocardial action potential, and loss-of-function mutations prolong cardiac repolarization. In this study, we investigated the efficacy and mechanism of ICA-105574, an hERG activator, in shortening the duration of cardiac repolarization in severe LQT2 variants. We characterized the *in vivo* efficacy of ICA-105574 in shortening the QT duration in an animal model and *in vitro* in enhancing I_{Kr} current in cellular models mimicking severe hERG channel mutations (A561V, G628S, and L779P). We then used molecular dynamics simulations to investigate the molecular mechanism of ICA-105574 action. *In vivo*, ICA-105574 significantly shortened the QT interval. LQT2 mutations drastically reduced I_{Kr} amplitude and suppressed tail currents in cellular models. ICA-105574 restored I_{Kr} in A561V and G628S. Finally, *in silico* data showed that ICA-105574 stabilizes a pattern of interactions similar to gain-of-function SQT1 mutations and can reverse the G628S modifications, through an allosteric network linking the binding site to the selectivity filter and the S5P turret helix, thereby restoring its K^+ ion permeability. Our results support the development of hERG activators as pharmacological molecules against some severe LQT2 mutations and suggest that molecular dynamics simulations can be used to test the ability of molecules to modulate hERG function *in silico*, paving the way for the rational design of new hERG activators.

Introduction

The *KCNH2* gene encodes a voltage-gated K^+ channel (human ether-à-go-go, hERG) in neurons and cardiac cells. Its primary role involves cardiac repolarization through the rapid delayed rectifier K^+ current (I_{Kr}), which significantly influences the duration of the QT interval on the surface electrocardiogram (ECG) (*1*, *2*). Abnormalities in the hERG channels are characterized by two distinct cardiac disorders, namely Long QT Syndrome (LQTS) and Short QT Syndrome (SQTS), which manifest as the prolongation or the shortening of the QT interval on the ECG. Congenital LQTS accounts for nearly 40% of cases (*3*, *4*), while the majority of LQTS cases stem from pharmacological blockade by various clinically used drugs. Mutations in hERG channels can result in a loss of function due to defective trafficking, abnormal channel gating or reduced ion permeation. Notably, approximately 90% of LQT syndrome type 2 (LQT2) mutants exhibit reduced synthesis and defective trafficking (*5*, *6*), yet certain mutations (e.g. G628S, N629D) (*7*, *8*) near the selectivity filter (SF) can maintain normal trafficking while failing to exhibit ion selectivity and conductance in physiological solutions. On the other hand, SQT type 1 (SQT1) mutations (e.g. N588K, T618I, S631A) are often associated with reduced or loss of inactivation, resulting in a shorter QT interval (*9*, *10*). The large number of LQT2-associated missense mutations distributed throughout the hERG sequence poses a challenge to pharmacological treatments. Of note, Priori and coworkers showed that substrate-specific therapy with mexiletine, which shortens the QT interval, confers arrhythmic protection in LQT3 (*11*, *12*). This suggests that, in principle, QT interval shortening is an effective strategy for the treatment of LQT2. This could be achieved with hERG activators (*13*), which enhance the rapid component of the delayed rectifier K^+ current (I_{Kr}) and may be able to shorten the duration of cardiac repolarization in LQT2.

Structurally, hERG channel is a homotetramer consisting of an N-terminal cytosolic Per-Arnt-Sim (PAS) domain followed by six transmembrane segments: S1-S4, forming the voltage-sensing domain (VSD), and S5-S6, together with the S5P turret region and the P helix, forming the pore-forming domain (PD); and the C-terminal cyclic nucleotide-binding homology domain (CNBHD), all intertwined by long disordered regions (*14*). The hERG channel undergoes critical kinetic transitions between its closed (deactivation), active and inactivated states that regulate cardiac repolarization. Despite the recently available cryo-EM structure, the distinctive mechanism of rapid inactivation and recovery, and slow deactivation remains poorly understood due to the limited structural information available for the closed and inactivated states and are mostly the results of indirect indications obtained from homologues (*15*–*19*). A recently determined cryo-EM structure for the hERG-astemizole complex has confirmed the general understanding that blockers bind to a hydrophobic pocket at the entrance of the SF, thus blocking the passage of K^+ ions, and provides further tools for structure-based screening of hERG-related cardiotoxicity (*20*–*23*).

While hERG drug screening is primarily focused on the identification of drug-induced arrhythmic compounds, it has also revealed agonists (activators) that can enhance the outward current I_{Kr} amplitude (*24*). These compounds show distinct mechanisms of action, with the majority inhibiting C-type inactivation, while others delay deactivation, increase channel open probability, or exhibit a combination these effects. From a structural perspective, these compounds appear to target different regions of the protein while avoiding blocking the channel (*25*). Several activators have been investigated as potential candidates for different congenital LQTS mutations representing a novel approach to the prevention of ventricular arrhythmias associated with LQTS (*25*). However, they carry the risk of inducing early repolarization, leading to an excessive correction of action potential duration (APD), which could ultimately shorten the QT interval to proarrhythmic levels (i.e., SQT). One such compound is ICA-105574, a derivative of 3-nitro-n-(4-phenoxyphenyl) benzamide, that is the most potent I_{Kr} activator to date (*26*, *27*). Previous experimental and computational studies have revealed its binding site within a hydrophobic pocket located between two adjacent subunits, where it interacts with residues in the pore

helix, the base of the SF, and the S6 segments (*28–30*). ICA-105574 is proposed to act through a subtle change in the configuration of the selectivity filter that disrupts inactivation gating, with a demonstrated stoichiometric dependence where binding of multiple ICA-105574 molecules is required for optimal activity of the compound (*31*).

In this study, we employed a multi-pronged approach using *in vivo* and *in vitro* electrophysiology and molecular dynamics (MD) simulations to explore the therapeutic potential and mechanism of action of ICA-105574 in LQT2 and in severe hERG mutations, specifically A561V, G628S, and L779P, derived from our cohort of LQT2 patients. First, we validated *in vivo* the ability of ICA-105574 to rescue QT prolongation in a sotalol-induced animal model mimicking LQT2. Then, we subcloned and expressed the above mentioned severe LQT2 hERG mutations in specific established stable cell lines to study their functional activity on current amplitude before and after ICA-105574 treatment, with our results indicating that ICA-105574 restores I_{Kr} amplitude in cellular models (A561V and G628S). Finally, we performed MD simulations to elucidate the molecular mechanisms of action of ICA-105574 in both wild-type and mutant hERG channels. There we revealed how ICA-105574 can rescue the permeability to K^+ of the G628S mutation by stabilizing a pattern of interactions analogous to that observed in simulations of two SQT1 mutations (i.e., N588K and S631A) through an allosteric network connecting distant regions of the protein. Our results allow us to propose that *in silico* methods are now sufficiently mature to evaluate molecules based on their ability to rescue channel conductance, indicate a molecular framework that can be used to rationalize its mechanism of action, and provide valuable insights into the therapeutic potential of ICA-105574.

Results

In vivo electrophysiological experiments demonstrate the shortening of the QT interval mediated by ICA-105574

To evaluate the efficacy of ICA-105574 in shortening the QT interval in LQT2 patients, we performed *in vivo* electrophysiological experiments by recording the ECG signal in conscious guinea pigs. Our choice was primarily due to different issues: 1) to enroll the animal model with the cardiac electrophysiological phenotype as closely as possible to human; 2) to avoid any possible effect of the anesthetic on the sensitivity to drug (*32*, *33*) ; 3) to observe any possible side effects in free moving animals; 4) to employ the smallest animal model with an easily recognizable T wave requiring the smallest amount of drug possible. To combine all the above reported aspects, we decided to employ the guinea pigs, since their cardiac ion currents are similar to humans (*34*), with an easily identifiable P, Q, R, S and T waves recapitulating the LQT2 phenotype.

We investigated the effect of the I_{Kr} activator ICA-105574 in a chemically induced LQT2 guinea pig. The LQT2 condition was mimicked by pre-treating the guinea pig with 50 mg/Kg of sotalol, with a pronounced prolongation of the QTc interval from a baseline of 255 ms (IQR: 252-259 ms) was consistently obtained in all guinea pigs (ΔQTc +41 ms, +17%; <0.001) (35–37). Despite marked QTc prolongation, during the electrocardiographic registration no spontaneous arrhythmic events were observed. Following the demonstration of successful induction of LQT2, a single intraperitoneal dose of ICA-105574 at 15 mg/Kg was administered. Immediately upon drug administration, QTc interval normalization was consistently obtained in all guinea pigs (ΔQTc -43 ms, -14%; <0.001). This effect was transient and by 30 minutes after administration QTc interval normalization waned with QTc lengthening back to values comparable to ones prior to ICA-105574 administration. No other biologically significant effects on the principal electrocardiographic parameters were observed (Figure 1).

In vitro electrophysiological analysis of ICA-105574 with, A561V, G628S and L779P

We then characterized the functional properties of hERG mutations (A561V, G628S and L779P) and their response to ICA-105574 as an I_{Kr} activator. We generated chimeric proteins (pmCherry-N1-hERG-WT, -A561V, -G628S and -L779P) and established single stable cell lines for each condition to perform electrophysiological studies following ICA-105574 perfusion. The pmCherry-N1-hERG-WT was transiently transfected into HEK293 cells and protein expression was assessed by Western blot and localized by confocal microscopy. These preliminary analyses confirmed the correct expression of the chimera and its distribution along the cell membrane (SI Appendix Figure S1). Similarly, we generated and performed the experiments for all the hERG mutations (SI Appendix Figure S2). Both mCherry-N1-hERG-A561V and -G628S were stained along the plasma membrane with some diffuse staining in the cytoplasm, similar to the hERG-WT. In contrast, the hERG-L779P was mainly localized in the cytoplasm, with enrichment around the perinuclear region. The localization of all hERGs proteins were not affected by ICA-105574 treatment.

To define the functional change of ICA-105574 on LQT2 mutations, electrophysiological analysis was performed in HEK293 stable cell lines expressing hERG-WT and mutants (A561V, G628S, L779P). I_{Kr} was elicited by the voltage-clamp protocol showed in figure S3 in control conditions and in presence of 10 µM ICA-105574. From a holding potential of -80 mV, voltage pulses were applied to voltages ranging from -60 to +70 mV with delta of 10 mV and repolarized at -60 mV. By this activation protocol, it was possible to note that the functionality of the hERG channels was impaired by the fact that the mutations induced a suppression of the tail currents, making impossible the calculation of the activation curve parameters ($V_{1/2}$ and slope) to evaluate the voltage dependence of hERG channel activation (as in Sanguinetti et al. for A561V and G628S (*38*)). The A561V mutation reduced the steady state pre-pulse current amplitude and only partially distorted the hERG current behavior (Figure 2), whereas the effect of G628S and L779P led to a drastic reduction of the I_{Kr} current amplitude at all voltages (Figure 2 and SI Appendix Figure S3). In particular, the G628S and L779P mutations produced currents that did not reach a peak and a plateau phase and this avoided to obtain a bell-shape curve in the I/V activation relationship typical of WT. Taken together, these data allow us to speculate that G628S and L779P negatively altered channel opening, in agreement with previous data for G628S (*8*, *30*, *38*, *39*).

The hERG stable cell lines (WT, A561V, G628S, L779P) were perfused with ICA-105574 (10 µM). The treatment induced a strong I_{Kr} activation on steady state currents in both WT and A561V (from 0 or -20 to +70 mV, respectively) and G628S (from -30 to +70 mV) partially restoring the functionality of the mutated channels. Notably, both the A561V and G628S mutations showed a statistically significant positive response to ICA-105574 (Figure 2 and S3) demonstrated by: 1) the increase of current amplitude in the I/V relationship (in A561V the peak is more than quadrupled in size); 2) the change of the shape of the I/V relationship, which exhibited a rectification, partially resembling the WT one (Figure 2). In A561V a complete bell-shaped curve was obtained, while in G628S the straight bent until to look like a half bell-shaped curve. This suggests that the I_{Kr} activator treatment could be able to induce an increment of the outward currents during the action potential plateau phase leading to acceleration of ventricular repolarization and a reduction in the duration of action potential and consequently shortening the QT phase. This is the first study demonstrating that A561V and G628S hERG mutations are responsive to ICA-105574 perfusion. Conversely, the hERG-L779P did not respond to ICA-105574, where I_{Kr} amplitude is not increased and I/V activation curve did not undergo any change of shape, suggesting that ICA-105574 does not induce any alteration in hERG protein' conformation, preventing channel opening.

Restrained Molecular Dynamics allow simulating the hERG active state

Having shown that ICA-105574 can rescue the activity of G628S and A561V but not that of L779P *in vitro*, we set out to understand the molecular determinants of this rescue mechanism using MD simulations. Previous work on the hERG channel showed rapid inactivation on the ns time scale for the wild-type protein, making it difficult to accumulate extensive statistics on the conformational dynamics of the hERG active state (*15*, *16*, *40*). Here we started with a known cryo-EM structure (PDB ID: 5VA2) determined in the active state for the wild type (Figure 3A), including the PAS domain (18), in a POPC bilayer with 200 mM salt concentration (KCl) and applied transmembrane voltage ranging from ~650 mV to ~750 mV. In a first round of preliminary simulations (SI Appendix Table S1A), we observed, in agreement with the work of Miranda et. al. (*40*), a fast inactivation on the ns time scale, manifested by the flipping of carbonyl oxygen atoms and subsequent SF distortion (SI Appendix Figure S4). The fast kinetics of these structural changes could be attributed to the use of a high electric field and to inaccuracies in the force field parameters. Therefore, to ensure that the selectivity filter remains stable during the simulations, we restrained the backbone torsion angles (φ, ψ). The resulting systems show a stable SF over the course of the restrained MD simulations, (SI Appendix Figure S4), with the diameter between opposite chains in agreement with cryo-EM reference values for highly flexible F627, while with a small dilation for S624 and V625 residues.

Ion permeation mechanisms in potassium ion channels have been found to be ambiguous in nature, depending on the type of force field considered, the membrane potential, and the charge corrections for the ions (*41*). In preliminary simulations with dihedral restraints (SI Appendix Table S1B), we observed mostly a soft knock-on mechanism for the ion permeations using the CHARMM force field with NBFIX parameters (*42*), regardless of the initial configuration of the ions ([KKKKK] or [KWKWK]). In addition, the mixed KCl and NaCl simulations for the wild-type system established the ion selectivity with outward K^+ ion movement and no inward/outward Na^+ ion movement in the presence of torsional restraints. Therefore, subsequent production simulations were run with [KWKWK] ion configuration and KCl salt only for uninterrupted ion permeations (see SI Appendix Movie S1 and Table S2). Simulations were performed for six systems containing LQT2 and SQT1 mutations, namely WT, G628S, WT-ICA, G628S-ICA, S631A, and N588K. WT and G628S simulations, with and without ICA-105574, were performed to observe and characterize the molecular determinants of ICA-105574-induced hERG rescue. While N588K and S631A represent SQT1 mutations used in this work to investigate whether the effect of ICA-105574 is structurally comparable to that of these pathological mutations, given their associated attenuated inactivation (*9*, *10*). To demonstrate the effect of ICA-105574, two molecules were docked into the opposite subunit fenestrations based on the previously identified binding site residues (*28–30*) (Figure 3B, cf. SI Appendix for the molecular docking protocol). The rationale for using two ICA-105574 molecules is based on earlier study suggesting that a single ICA molecule binding to a subunit is insufficient to enhance channel activity (*28*). ICA-105574 is found to be stable in WT-ICA and G628S-ICA systems over the course of simulations (SI Appendix Figure S5A, B). Our energetic analysis reveals that ICA-105574 molecules forms favorable polar and non-polar interactions in the form of H-bond (S649) and pi-pi interactions (F557, Y652, F656) in the respective fenestrations (SI Appendix Figure S5C, D).

Ion permeation and selectivity filter stability as a feature of active state

Because of the stable SF resulting from our restrained MD simulations, we recorded continuous K^+ ion permeation events in multiple trajectories for all systems except, remarkably, the LQT2-G628S system. Based on these trajectories, we calculated the ion occupancy probability at different sites in the selectivity filter described previously for K^+ ion channels (Figure 4A). All ion-permeable systems show higher ion occupancy at the S2 site, which in turn prevents the collapse of SF (*43*). In contrast, the ion occupancy at S2 decreases in LQT2-G628S, which is restored in the presence of ICA-105574 in the G628S-ICA system. The number of ion permeations varies in the multiple replicates of each system (SI

Appendix Table S2). Therefore, we estimated an average transition time (τ) for an ion to permeate through the SF from S-cavity to the escape of the ion from the S0 site (Figure 4B). The average transition time of a single ion permeation event for WT, S631A, and ICA-bound systems (WT-ICA, G628S-ICA) is in the range of 100-150 ns, with the exception of 260 ns for N588K (Figure 4B, inset), suggesting that our MD simulations cannot fully capture the differences in conductance, possibly due to a combination of force field limitations and the high applied membrane potential. Despite these approximations, our model can capture the loss of conductance in terms of ion permeations across the SF in G628S and, remarkably, the rescue effect of ICA-105574 in the G628S-ICA system in agreement with our *in vitro* electrophysiological data (Figure 2). These observations suggest that we can interrogate our MD simulations to obtain relevant structural information on the rescue mechanism. Importantly, previous *in silico* studies (*28*, *44*) of hERG activators have never explicitly demonstrated the effect of these molecules on conductance.

The helicity of the S5P turret as a signature of activation propensity

Structural and computational studies suggest that the active state of the hERG channel differs from inactivation in terms of the diameter of the SF and the heterogeneity in the dihedral angles of F627 (*19*, *40*). In a recent preprint, Vanderberg and coworkers report the narrowing of the SF in the cryo-EM structure of hERG in the inactivated state (*45*). In our simulations, the average diameter for the SF residues is found to be stable and similar for wild-type, SQT mutations (N588K, S631A), and WT-ICA systems (Figure 4C). While, in the presence of LQT mutation (G628S), there is a notable increase in the diameter around F627 (0.80 ± 0.1 nm) and S628 (1.13 ± 0.08 nm) showing the effect of the mutation. Of note, the G628S-ICA bound system showed only a small decrease in the SF diameter with respect to G628S, suggesting that in this range of values, SF diameter is not a clear signature of activation. To access any major conformational rearrangements and flexibility in the pore domain (PD) upon mutation or ligand binding, we analyzed the inter-residue pairwise distances for different systems with respect to the wild type (SI Appendix Figure S6 A-E). Overall, no major conformational changes in the pore domain were observed, except for a higher flexibility in the extracellular loops in the wild type and G628S as compared to the other systems (SI Appendix Figure S6F), suggesting that the differences we are looking for may be subtle and related to the conformational dynamics of the system. In hERG, experimental evidence emphasizes on the role of the S5P turret helix (residues 584-592) in the c-type inactivation mechanism (*46–48*), and the S5P segment has been observed to exist between helical and unstructured conformations in MD simulations. Interestingly, we observe a clear trend in the helicity of this region within SQT mutations and ligand-bound hERG channel as compared to the wild type (Figure 4D). Importantly, the G628S mutation has the least helical propensity, which is restored in the presence of ICA-105574. The activator is proposed to act primarily by attenuating rapid inactivation by increasing the stability of SF and channel conductance; it is intriguing how the binding of ICA-105574 below the SF can exert its function via conformational changes at long distance in the S5P turret helix. In contrast both SQT mutations are localized within or in contact with this region (Figure 3A) and may alter its role in c-type inactivation.

ICA-105574 promotes molecular interactions and hydrogen bond rearrangement in the rescue state

So far, our observations suggest the signatures of the rescue effect in the G628S-ICA system; therefore, we now investigate the molecular mechanism of the rescue effect of the ICA-105574 in the G628S mutation. We calculated the variation of the hydrogen bond (H-bond) occupancy in the pore domain of the hERG channel in the wild-type, G628S, and activator-bound G628S-ICA systems to identify changes in molecular interactions upon different perturbations (mutation or ligand binding). The net H-bond occupancy (%) between two residues i and j is given by $\Delta HB_{ij} = HB_{ij}^{perturbation} - HB_{ij}^{reference}$

where the perturbation factor could be mutation or ligand binding while the reference could be either WT or G628S. As shown in Figure 5, red lines indicate residue pairs with higher H-bond occupancy (%) in the perturbed system, while blue lines indicate the same in the reference system (H-bond loss in perturbed system). When comparing G628S with WT, the analysis is the result of an averaging over the four chains (Figure 5A), whereas when comparing G628S with G628S-ICA, we had to take into account the asymmetric docking of the activator across two adjacent monomers, so we have analyzed the change in the H-bond occupancy in these chains separately (Figure 5B). Our analysis showed that the G628S mutation decreases the H-bond occupancy around the SF (F617-S621, S620-G626, S631-N633) and in the S5P turret helix spanning from G584 to Q592 as compared to the WT (Figure 5A). Notably, binding of ICA-105574 to the G628S system resulted in a marked increase in H-bond occupancy, in both adjacent chains, for residues around SF (Y616-S620, S620-G626) and in the S5P turret helix residues (G584-Q592). The asymmetric positioning of ICA-105574 also resulted in different H-bonding patterns in adjacent chains. For example, one chain had higher H-bond occupancy near SF (F617-S621, S621-S624) and W568-W585, while another chain with more ICA-105574 contacts had increased H-bond occupancy in the S6 helical subunit. In addition, some residue pairs (e.g. Y616-N629, E637-S641, M645-S649 and at the S6 helix end) have higher H-bond occupancy in G628S than in WT (Figure 5A, red lines). However, this difference is reversed when ICA-105574 binds to G628S (Figure 5B, red lines). Notably, we also observed a similar H-bond rearrangement in the S5P turret region when comparing the WT and WT-ICA systems (SI Appendix Figure S8A), supporting that this is a robust feature of ICA-105574 binding. Furthermore, a similar pattern is observed when comparing the WT with the S631A and N588K SQT variants (Figure 5 C, D). Overall, the increase in turret helicity (Figure 4D) and the decrease in RMSF (SI Appendix Figure S6F) observed above for both ICA-105574 bound and SQT systems can be attributed to a rearrangement of H-bonds occupancy, although the mechanism of stability may differ between systems. For example, the mutation of the polar amino acid (N588) to a charged amino acid (K588) increases helix stability by forming a salt bridge with D591, whereas mutation of S631A replaces the wild-type S631-N633 H-bond with an N588-A631 H-bond.

While these observations further highlight a similarity between the binding of ICA-105574 and two SQT mutations under study, they still do not fully describe how ICA-105574 may exert its long-range effect on the conformational dynamics of hERG. To this end, we focused on a single monomer chain and shortlisted residues with either higher net H-bond occupancy in G628S-ICA or $E_{i,ICA} < -2.5\ kcal/mol$ (SI Appendix Figure S5D). We identified S624 as a common residue in this list and defined it as the starting point of the allosteric network, coupling ICA-105574 to the SF and the S5P turret helix. Specifically, we observed that the nitro group of ICA-105574, located behind the SF, formed favorable interaction with the hydroxyl group of S624 (Figure 6A). This resulted in a population shift of the chi (χ_1) dihedral angle of S624, which describes the orientation of its side chain (Figure 6B). We hypothesize that this favorable interaction may trigger a domino effect in the form of an increase in the H-bond occupancy of several neighboring residue pairs behind the SF (Y616-S620, S620-G626), as previously shown in Figure 5, including A561-T618, F617-S621, S621-S624, with some of these occupancy changes manifesting as a significant shift in side chain orientation (e.g. T618, S620) upon ICA-105574 binding (Figure 6C). In particular, the changes observed for the region S620-S624 and the S5P turret helix are associated with a population shift in the χ-dihedral distribution of F617 and the tryptophan clamp (W568-W586). In Figure 7, we have shown a 2D distribution of the χ_1/ χ_2 angle in the residue pairs W568-F617 (Figure 7A, B) and W568-W585 (Figure 7C, D). Here, we observed that the population density of the χ dihedrals for W568-F617 increases for a basin (F617(χ_2) ~ -100°, W568(χ_1) ~180°) without changing the overall shape of the distribution. While in the case of W568-W585, there is a marked shift for W585 (χ_1) towards exclusively side chain orientation upon ICA-105574 binding, whereas the population for W568 (χ_1) dihedral is significantly higher in one state (~180°) in G628S-

ICA compared to the G628S system. Thus, the pairing in the side chain orientations of these three residues may enhance the interaction between the S5, pore helix, and turret region in the activated state. These results are consistent with what we have observed *in vitro* for A561V and L779P. Indeed, the A561V mutation is located within the network identified here and its effect is consistently rescued by ICA-105574. In contrast, the L779P mutation is located in the cyclic nucleotide-binding homology domain (CNBHD), its effect cannot thus be interpreted by our conformational analysis, and it cannot be rescued by ICA-105574 (Figure 2). To test the extent to which MD simulations can capture the effect of additional mutations, we performed an additional round of simulations on the A561V and L779P systems.

MD simulations of A561V and L779P highlight strengths and limitations of our *in silico* approach

Regarding the A561V mutation located in the S5 helix of the pore domain, in our *in silico* model, both the A561V and A561V-ICA systems exhibited ion permeation comparable to the WT and all conducting systems studied here, with ion occupancy in the selectivity filter consistent with the above observations (Figure 4 and SI Appendix Figure S9). Interestingly, the permeation rate for A561V-ICA is the same as that observed for the WT-ICA and G628S-ICA systems, indicating some robustness. No obvious differences were observed in the SF due to this mutation (SI Appendix Figures S10, S11, and S12A). In addition, the helicity of the S5P turret suggests a conducting system with values greater than the WT. Notably, the A561V and A561V-ICA systems also show an increase in H-bond occupancy in the helical residues of the S5P turret (G584-Q592) and around SF (Y616-S620, S620-G626). These results suggest that the A561V mutation does not affect the active state. On the one hand, this may be consistent with our *in vitro* electrophysiological data showing that A561V reduces but does not drastically alter the steady state pre-pulse current amplitude and only partially distorts hERG current behavior. On the other hand, it highlights the limitations of our *in silico* model to capture the complexity of ionic conductance and current changes in mutant hERG channels by focusing only on the open state.

For the L779P mutation, located in the cyclic nucleotide-binding homology domain (CNBHD), we focused on simulating only the CNBHD of hERG channels (*49*) in both the wild-type and mutant states (SI Appendix for Materials and Methods). The L779 residue is strategically positioned within the central beta-strand of the beta-roll, which is a common fold among canonical cyclic nucleotide-binding proteins. It establishes favorable hydrophobic and backbone H-bond interactions with neighboring residues, thus contributing to the overall stability of this domain. However, the introduction of a proline mutation at position L779 can have a significant impact on the overall structure of the CNBHD. Interestingly, our simulations showed a significant increase in the RMSF for the CNBHD in the presence of the L779P mutation (SI Appendix Figure S12B). The dramatic increase in fluctuations observed here, coupled with the loss of interactions in the inner core of the CNBHD, suggests a loss of stability in this domain, potentially increasing the risk of misfolding and a putative loss of functionality. This is consistent with our in vitro observations, where most of the protein is localized in the cytoplasm, with enrichment around the perinuclear region, suggesting some folding and trafficking defects. Having observed that the effect of ICA-105574 is primarily localized to the SF region, its inability to rescue such a mutation is therefore expected.

Discussion

LQTS predisposes young patients to develop ventricular fibrillation leading to sudden cardiac death. QT interval duration is a strong predictor of arrhythmic events, with each 10 ms increase conferring a 15% increased risk (*50*). We decided to test whether ICA-105574, an hERG activator, could be a good candidate to shorten the duration of cardiac repolarization in LQT2, by gaining an insight at three different levels: *in vivo*, *in vitro* and *in silico*. Our combined data allow to suggest that A561V, G628S and L779P mutants act on different aspects of hERG function, with A561V possibly stabilizing states

other than the active one, G628S clearly disrupting the conductivity of the open state and L779P by strongly destabilizing the CNBHD domain. Importantly, our *in vitro* data showed that the I_{Kr} activator ICA-105574 can rescue the function of A561V and G628S hERG LQT2 mutations by a mechanism similar to that of some known SQT1 mutations (i.e., S631A and N588K). ICA-105574 binding stabilizes a network of amino acids in the SF, pore helix and S6 helix, allowing its effects to propagate ~2 nm away to the S5P turret helix. Interestingly, a significant number of LQT2 mutations fall in the pore region identified (*51*, *52*) and may be consistently rescued by ICA-105574. At the same time, we cannot exclude the efficacy of ICA-105574 against other mutations in heteromeric wild-type/mutant combinations that were not the focus of this work. Finally, the stabilization mechanism observed here is also compatible with the increased potency of the drug with increasing stoichiometry, as previously observed (*31*).

In conclusion, the *in vivo* experiments confirmed that administration of ICA-105574 induced a pronounced and statistically significant shortening of the QT interval in LQT2 and, importantly, no arrhythmic events were observed. In parallel, our *in vitro* analyses showed that the I_{Kr} activator can partially rescue and restore the functionality of specific hERG LQT2 mutations. Thus, we support the hypothesis that hERG channel activators may represent a potentially very powerful novel therapeutic strategy for LQT2 patients. Furthermore, we note that molecular dynamics simulations such as the one performed here, which focus on the functional effect of a drug, despite all their approximations, are optimally positioned to provide an *in silico* platform to test the functionality of hERG activators even in the difficult case of testing a drug rescue mechanism.

Materials and Methods

A summary of the different materials and methods used in this study is given below. More detailed descriptions are provided in the supplementary information.

ICA-105574 preparation

ICA-105574 was synthesized following a recently reported procedure by Zangerl-Plessl et al. (*28*), which is also employed in our recently published study (53*).*

In vivo electrophysiological experiments

The procedures employing Guinea pigs (Dunkin Hartley) were approved by the Ministero Italiano della Salute (Rome, Italy; 854/2019-PR). We used D,L-Sotalol (50 mg/Kg) to develop a drug-induced model of LQT2. The ECG signal was recorded for 90 minutes, ICA-105574 (15 mg/Kg) was intraperitoneally administered, and the ECG signal was recorded for 90 minutes after injection. The QTc interval value was corrected for heart rate by the Bazett's formula (*35*). The ECG parameters were evaluated by a mixed effects model, using RStudio 11 Version 4.1.1 (Boston, MA, USA). The significance level was considered at $p < 0.05$.

Cloning of hERG-WT and mutants in heterologous systems

The commercial clone of full-length human hERG (NM_000238.3) cloned in pCMV6-XL4 (Origene) was subcloned in pmCherry-N1 (Clontech) to generate a functional chimera. Site-direct mutagenesis was performed using QuickChange II XL kit (Agilent Technologies) to generate the single hERG mutations: pmCherry-N1-hERG-A561V, pmCherry-N1-hERG-G628S and pmCherry-N1-hERG-L779P. All the plasmids were entirely sequenced. Primers are indicated in the supplementary information.

Cell culture and transfection

The HEK293 stable cell lines were generate by a transfection with Effectene (Qiagen) and 1µg plasmid (pmCherry-N1-hERG-WT and -A561V, -G628S and -L779P, respectively) and selected by G 418

Sulfate (Calbiochem) and the hERG-mCherry-positive cells were sorted by BD FACS Aria III (Becton Dickinson)

Immunofluorescence

HEK293 cells with pmCherry-N1-hERG-WT or mutants (A561V, G628S or L779P) were stained with antibodies indicated in the supplementary materials and analyzed by confocal microscopy.

Protein extraction and Immunoblotting

48h after transient transfection, HEK293 cells have been lysated in RIPA buffer; 30 µg of total proteins, were quantified and resolved by SDS-gel electrophoresis and blotted on 0.2 µm nitrocellulose membrane.

In vitro electrophysiological experiments

Electrophysiological recordings were performed on stable HEK293 cell lines expressing the single mCherry mutation were chosen for current recordings. The solutions are the same used in Milani et al. (*54*). All data were tested by two-way ANOVA with an appropriate post-hoc correction (Šidák test). Two-tailed p values were calculated with the statistical significance threshold set at $p < 0.05$.

Molecular docking and simulations details

MD simulations were performed for six systems. These systems included wild type (WT, PDB: 5VA2), two SQT mutations (N588K and S631A (PDB: 5VA3)), two LQT2 mutations (A561V and G628S), and complexes of ICA-105574 with WT and LQT2 mutated channels. The ICA-105574 molecules were positioned within the channel using the Schrödinger Glide software for molecular docking. In addition, MD simulations for the Cyclic Nucleotide-Binding Homology Domain (CNBHD, PDB: 2N7G) were performed to assess the impact of the LQT2 mutation L779P on the domain's stability and conformation. All the simulations in the present study were performed using GROMACS (*55*) with the CHARMM36 forcefield (*56*) and the TIP3P water model (*57*). Further details about molecular docking and simulations are described in the supplementary information.

Acknowledgments

The authors thank Amanda Oldani, Patrizia Vaghi and Samantha Solito for technical assistance provided to the confocal microscopy and the cytofluorimetry facility, respectively, and “Centro Grandi Strumenti” of the University of Pavia. We also acknowledge a CINECA award under the ISCRA initiative (HP10C4059K), for the availability of high-performance computing resources and support and EuroHPC JU for awarding this project access to Lumi-C (EHPC-REG-2022R01-041) at CSC in Kajaani, Finland. The guinea pig and syringe images in Figure 1A were created using BioRender 2024 from BioRender.com. License Number: TR26ZK0LX7.

Funding

The work in this manuscript was supported by Fondazione Telethon - Italy (Grant #GGP19134) awarded to Silvia G. Priori and Carlo Camilloni.

Author contributions

AK performed and analyzed molecular dynamics simulations; ET performed and analyzed in vitro experiments and performed the in vivo experiments; GL synthesized and developed the formulation for in vivo and in vitro delivery of the ICA-105574 compound; AT and DK performed and analyzed in vivo experiments; MD performed and analyzed the molecular biology experiments and performed the in vivo experiments; AK, ET, SGP, and CC wrote the manuscript with contributions from all authors; SGP and

CC designed and supervised the project and provided resources. All authors have given approval to the final version of the manuscript. ‡These authors contributed equally.

Competing interests

All other authors declare they have no competing interests.

Data and materials availability

The MD simulations data generated and analyzed in the current study can be accessed on Zenodo: https://zenodo.org/records/8349178.

Supplementary materials

The detailed information of materials and methods, additional supporting figures are available as separate file (Supporting Information). An illustration of the movement of potassium ions through the selectivity filter is shown in the form of a movie (mpg).

References

1. M. E. Curran, I. Splawski, K. W. Timothy, G. M. Vincen, E. D. Green, M. T. Keating, A molecular basis for cardiac arrhythmia: HERG mutations cause long QT syndrome. Cell 80, 795–803 (1995).
2. A. Zou, M. E. Curran, M. T. Keating, M. C. Sanguinetti, Single HERG delayed rectifier K+ channels expressed in Xenopus oocytes. Am J Physiol 272 (1997).
3. M. C. Sanguinetti, C. Jiang, M. E. Curran, M. T. Keating, A mechanistic link between an inherited and an acquird cardiac arrthytmia: HERG encodes the IKr potassium channel. Cell 81, 299–307 (1995).
4. L. Crotti, G. Celano, F. Dagradi, P. J. Schwartz, Congenital long QT syndrome. Orphanet J Rare Dis 3, 1–16 (2008).
5. C. L. Anderson, B. P. Delisle, B. D. Anson, J. A. Kilby, M. L. Will, D. J. Tester, Q. Gong, Z. Zhou, M. J. Ackerman, C. T. January, Most LQT2 Mutations Reduce Kv11.1 (hERG) Current by a Class 2 (Trafficking-Deficient) Mechanism. Circulation 113, 365–373 (2006).
6. J. L. Smith, C. L. Anderson, D. E. Burgess, C. S. Elayi, C. T. January, B. P. Delisle, Molecular pathogenesis of long QT syndrome type 2. J Arrhythm 32, 373–380 (2016).
7. J. P. Lees-Miller, Y. Duan, G. Q. Teng, K. Thorstad, H. J. Duff, Novel gain-of-function mechanism in K(+) channel-related long-QT syndrome: altered gating and selectivity in the HERG1 N629D mutant. Circ Res 86, 507–513 (2000).
8. Z. Zhou, Q. Gong, M. L. Epstein, C. T. January, HERG Channel Dysfunction in Human Long QT Syndrome. Journal of Biological Chemistry 273, 21061–21066 (1998).
9. A. Butler, Y. Zhang, A. G. Stuart, C. E. Dempsey, J. C. Hancox, Action potential clamp characterization of the S631A hERG mutation associated with short QT syndrome. Physiol Rep 6 (2018).
10. M. J. McPate, R. S. Duncan, J. T. Milnes, H. J. Witchel, J. C. Hancox, The N588K-HERG K+ channel mutation in the 'short QT syndrome': Mechanism of gain-in-function determined at 37°C. Biochem Biophys Res Commun 334, 441–449 (2005).
11. S. G. Priori, C. Napolitano, F. Cantù, A. M. Brown, P. J. Schwartz, Differential response to Na+ channel blockade, beta-adrenergic stimulation, and rapid pacing in a cellular model mimicking

the SCN5A and HERG defects present in the long-QT syndrome. Circ Res 78, 1009–1015 (1996).

12. A. Mazzanti, R. Maragna, A. Faragli, N. Monteforte, R. Bloise, M. Memmi, V. Novelli, P. Baiardi, V. Bagnardi, S. P. Etheridge, C. Napolitano, S. G. Priori, Gene-Specific Therapy With Mexiletine Reduces Arrhythmic Events in Patients With Long QT Syndrome Type 3. J Am Coll Cardiol 67, 1053–1058 (2016).

13. M. C. Sanguinetti, HERG1 Channel Agonists and Cardiac Arrhythmia. Curr Opin Pharmacol 0, 22 (2014).

14. J. I. Vandenberg, M. D. Perry, M. J. Perrin, S. A. Mann, Y. Ke, A. P. Hill, H. A. hERG K, hERG K CHANNELS: STRUCTURE, FUNCTION, AND CLINICAL SIGNIFICANCE. Physiol Rev 92, 1393–1478 (2012).

15. J. Li, R. Shen, B. Reddy, E. Perozo, B. Roux, Mechanism of C-type inactivation in the hERG potassium channel. Sci Adv 7 (2021).

16. F. Pettini, C. Domene, S. Furini, Early Steps in C-Type Inactivation of the hERG Potassium Channel. J Chem Inf Model 63, 251–258 (2023).

17. F. Costa, C. Guardiani, A. Giacomello, Molecular dynamics simulations suggest possible activation and deactivation pathways in the hERG channel. Communications Biology 2022 5:1 5, 1–11 (2022).

18. W. Wang, R. MacKinnon, Cryo-EM Structure of the Open Human Ether-à-go-go-Related K+ Channel hERG. Cell 169, 422-430.e10 (2017).

19. K. Ngo, V. Yarov-Yarovoy, C. E. Clancy, I. Vorobyov, Harnessing AlphaFold to reveal state secrets: Prediction of hERG closed and inactivated states. bioRxiv, 2024.01.27.577468 (2024).

20. T. Asai, N. Adachi, T. Moriya, H. Oki, T. Maru, M. Kawasaki, K. Suzuki, S. Chen, R. Ishii, K. Yonemori, S. Igaki, S. Yasuda, S. Ogasawara, T. Senda, T. Murata, Cryo-EM Structure of K+-Bound hERG Channel Complexed with the Blocker Astemizole. Structure 29, 203-212.e4 (2021).

21. S. Ekins, W. J. Crumb, R. Dustan Sarazan, J. H. Wikel, S. A. Wrighton, Three-Dimensional Quantitative Structure-Activity Relationship for Inhibition of Human Ether-a-Go-Go-Related Gene Potassium Channel. Journal of Pharmacology and Experimental Therapeutics 301, 427–434 (2002).

22. T. M. Creanza, P. Delre, N. Ancona, G. Lentini, M. Saviano, G. F. Mangiatordi, Structure-Based Prediction of hERG-Related Cardiotoxicity: A Benchmark Study. J Chem Inf Model 61, 4758–4770 (2021).

23. A. Cavalli, E. Poluzzi, F. De Ponti, M. Recanatini, Toward a pharmacophore for drugs inducing the long QT syndrome: Insights from a CoMFA study of HERG K+ channel blockers. J Med Chem 45, 3844–3853 (2002).

24. P. Z. Zhou, J. Babcock, L. Q. Liu, M. Li, Z. B. Gao, “Activation of human ether-a-go-go related gene (hERG) potassium channels by small molecules” in Acta Pharmacologica Sinica (2011)vol. 32, pp. 781–788.

25. A. El Harchi, O. Brincourt, Pharmacological activation of the hERG K+ channel for the management of the long QT syndrome: A review. J Arrhythm 38, 554–569 (2022).

26. M. Asayama, J. Kurokawa, K. Shirakawa, H. Okuyama, T. Kagawa, J. I. Okada, S. Sugiura, T. Hisada, T. Furukawa, Effects of an hERG activator, ICA-105574, on electrophysiological properties of canine hearts. J Pharmacol Sci 121, 1–8 (2013).

27. A. C. Gerlach, S. J. Stoehr, N. A. Castle, Pharmacological Removal of Human Ether-à-go-go-Related Gene Potassium Channel Inactivation by 3-Nitro-N-(4-phenoxyphenyl) Benzamide (ICA-105574). Mol Pharmacol 77, 58–68 (2010).

28. E. M. Zangerl-Plessl, M. Berger, M. Drescher, Y. Chen, W. Wu, N. Maulide, M. Sanguinetti, A. Stary-Weinzinger, Toward a Structural View of hERG Activation by the Small-Molecule Activator ICA-105574. J Chem Inf Model 60, 360–371 (2020).

29. V. Garg, A. Stary-Weinzinger, M. C. Sanguinetti, ICA-105574 Interacts with a Common Binding Site to Elicit Opposite Effects on Inactivation Gating of EAG and ERG Potassium Channels. Mol Pharmacol 83, 805–813 (2013).

30. V. Garg, A. Stary-Weinzinger, F. Sachse, M. C. Sanguinetti, Molecular Determinants for Activation of Human Ether-à-go-go-related Gene 1 Potassium Channels by 3-Nitro-N-(4-phenoxyphenyl) Benzamide. Mol Pharmacol 80, 630–637 (2011).

31. W. Wu, F. B. Sachse, A. Gardner, M. C. Sanguinetti, Stoichiometry of altered hERG1 channel gating by small molecule activators. Journal of General Physiology 143, 499–512 (2014).

32. Y. Sakaguchi, A. Sugiyama, S. Takao, Y. Akie, A. Takahara, K. Hashimoto, Halothane Sensitizes the Guinea-Pig Heart to Pharmacological IKr Blockade: Comparison With Urethane Anesthesia. J Pharmacol Sci 99, 185–190 (2005).

33. A. Takahara, A. Sugiyama, K. Hashimoto, Reduction of repolarization reserve by halothane anaesthesia sensitizes the guinea-pig heart for drug-induced QT interval prolongation. Br J Pharmacol 146, 561–567 (2005).

34. A. E. Busch, K. Malloy, W. J. Groh, M. D. Varnum, J. P. Adelman, J. Maylie, The Novel Class III Antiarrhythmics NE-10064 and NE-10133 Inhibit Isk Channels Expressed in Xenopus Oocytes and Iks in Guinea Pig Cardiac Myocytes. Biochem Biophys Res Commun 202, 265–270 (1994).

35. S. Ruppert, T. Vormberge, B. W. Igl, M. Hoffmann, ECG telemetry in conscious guinea pigs. J Pharmacol Toxicol Methods 81, 88–98 (2016).

36. H. Numaguchi, F. M. Mullins, J. P. Johnson, D. C. Johns, S. S. Po, I. C. H. Yang, G. F. Tomaselli, J. R. Balser, Probing the interaction between inactivation gating and Dd-sotalol block of HERG. Circ Res 87, 1012–1018 (2000).

37. H. S. Rasmussen, M. J. Allen, K. J. Blackburn, G. S. Butrous, H. W. Dalrymple, Dofetilide, a novel class III antiarrhythmic agent. J Cardiovasc Pharmacol 20 Suppl 2, S96–S105 (1992).

38. M. C. Sanguinetti, M. E. Curran, P. S. Spector, M. T. Keating, Spectrum of HERG K+-channel dysfunction in an inherited cardiac arrhythmia. Proceedings of the National Academy of Sciences 93, 2208–2212 (1996).

39. M. R. Stump, Q. Gong, Z. Zhou, Isoform-Specific Dominant-Negative Effects Associated with hERG1 G628S Mutation in Long QT Syndrome. PLoS One 7, e42552 (2012).

40. W. E. Miranda, K. R. DeMarco, J. Guo, H. J. Duff, I. Vorobyov, C. E. Clancy, S. Y. Noskov, Selectivity filter modalities and rapid inactivation of the hERG1 channel. Proc Natl Acad Sci U S A 117, 2795–2804 (2020).

41. M. Jensen, V. Jogini, M. P. Eastwood, D. E. Shaw, Atomic-level simulation of current–voltage relationships in single-file ion channels. Journal of General Physiology 141, 619–632 (2013).

42. S. Y. Noskov, S. Berněche, B. Roux, Control of ion selectivity in potassium channels by electrostatic and dynamic properties of carbonyl ligands. Nature 2004 431:7010 431, 830–834 (2004).

43. C. Boiteux, D. J. Posson, T. W. Allen, C. M. Nimigean, Selectivity filter ion binding affinity determines inactivation in a potassium channel. Proc Natl Acad Sci U S A 117, 29968–29978 (2020).

44. F. Costa, R. Ocello, C. Guardiani, A. Giacomello, M. Masetti, Integrated Approach Including Docking, MD Simulations, and Network Analysis Highlights the Action Mechanism of the Cardiac hERG Activator RPR260243. J Chem Inf Model, doi: 10.1021/acs.jcim.3c00596 (2023).

45. C. H. Y. Lau, E. Flood, M. J. Hunter, B. J. Williams-Noonan, K. M. Corbett, C.-A. Ng, J. C. Bouwer, A. G. Stewart, E. Perozo, T. W. Allen, J. I. Vandenberg, Potassium dependent structural changes in the selectivity filter of HERG potassium channels. bioRxiv, 2023.12.14.571769 (2023).

46. J. Liu, M. Zhang, M. Jiang, G. N. Tseng, Structural and functional role of the extracellular S5-P linker in the HERG potassium channel. Journal of General Physiology 120, 723–737 (2002).

47. A. M. Torres, P. S. Bansal, M. Sunde, C. E. Clarke, J. A. Bursill, D. J. Smith, A. Bauskin, S. N. Breit, T. J. Campbell, P. F. Alewood, P. W. Kuchel, J. I. Vandenberg, Structure of the HERG K+ Channel S5P Extracellular Linker: ROLE OF AN AMPHIPATHIC α-HELIX IN C-TYPE INACTIVATION. Journal of Biological Chemistry 278, 42136–42148 (2003).

48. C. E. Clarke, A. P. Hill, J. Zhao, M. Kondo, R. N. Subbiah, T. J. Campbell, J. I. Vandenberg, Effect of S5P α-helix charge mutants on inactivation of hERG K+ channels. J Physiol 573, 291 (2006).

49. Y. Li, H. Q. Ng, Q. Li, C. B. Kang, Structure of the Cyclic Nucleotide-Binding Homology Domain of the hERG Channel and Its Insight into Type 2 Long QT Syndrome. Scientific Reports 2016 6:1 6, 1–10 (2016).

50. A. Mazzanti, R. Maragna, G. Vacanti, N. Monteforte, R. Bloise, M. Marino, L. Braghieri, P. Gambelli, M. Memmi, E. Pagan, M. Morini, A. Malovini, M. Ortiz, L. Sacilotto, R. Bellazzi, L. Monserrat, C. Napolitano, V. Bagnardi, S. G. Priori, Interplay Between Genetic Substrate, QTcDuration, and Arrhythmia Risk in Patients With Long QT Syndrome. J Am Coll Cardiol 71, 1663–1671 (2018).

51. J. D. Kapplinger, D. J. Tester, B. A. Salisbury, J. L. Carr, C. Harris-Kerr, G. D. Pollevick, A. A. M. Wilde, M. J. Ackerman, Spectrum and prevalence of mutations from the first 2,500 consecutive unrelated patients referred for the FAMILION® long QT syndrome genetic test. Heart Rhythm 6, 1297–1303 (2009).

52. C. L. Anderson, C. E. Kuzmicki, R. R. Childs, C. J. Hintz, B. P. Delisle, C. T. January, Large-scale mutational analysis of Kv11.1 reveals molecular insights into type 2 long QT syndrome. Nat Commun 5 (2014).

53. A. Porta-Sánchez, A. Mazzanti, C. Tarifa, D. Kukavica, A. Trancuccio, M. Mohsin, E. Zanfrini, A. Perota, R. Duchi, K. Hernandez-Lopez, M. E. Jáuregui-Abularach, V. Pergola, E. Fernandez, R. Bongianino, E. Tavazzani, P. Gambelli, M. Memmi, S. Scacchi, L. Pavarino, P. C. Franzone, G. Lentini, D. Filgueiras-Rama, C. Galli, D. J. Santiago, S. G. Priori, Unexpected impairment of

INa underpins reentrant arrhythmias in a knock-in swine model of Timothy syndrome. Nature Cardiovascular Research 2023 2:12 2, 1291–1309 (2023).

54. G. Milani, R. Budriesi, E. Tavazzani, M. M. Cavalluzzi, L. B. Mattioli, D. V. Miniero, P. Delre, B. D. Belviso, M. Denegri, C. Cuocci, N. P. Rotondo, A. De Palma, R. Gualdani, R. Caliandro, G. F. Mangiatordi, A. Kumawat, C. Camilloni, S. Priori, G. Lentini, hERG stereoselective modulation by mexiletine-derived ureas: Molecular docking study, synthesis, and biological evaluation. Arch Pharm (Weinheim), doi: 10.1002/ardp.202300116 (2023).

55. M. J. Abraham, T. Murtola, R. Schulz, S. Páll, J. C. Smith, B. Hess, E. Lindah, GROMACS: High performance molecular simulations through multi-level parallelism from laptops to supercomputers. SoftwareX 1–2, 19–25 (2015).

56. J. Huang, S. Rauscher, G. Nawrocki, T. Ran, M. Feig, B. L. De Groot, H. Grubmüller, A. D. MacKerell, CHARMM36m: An Improved Force Field for Folded and Intrinsically Disordered Proteins. Nat Methods 14, 71 (2017).

57. W. L. Jorgensen, J. Chandrasekhar, J. D. Madura, R. W. Impey, M. L. Klein, Comparison of simple potential functions for simulating liquid water. J Chem Phys 79, 926–935 (1983).

58. A. J. J. Wood, S. H. Hohnloser, R. L. Woosley, Sotalol. https://doi.org/10.1056/NEJM199407073310108 331, 31–38 (1994).

59. A. Gałecki, T. Burzykowski, Linear Mixed-Effects Models Using R. doi: 10.1007/978-1-4614-3900-4 (2013).

60. M. G. Kenward, J. H. Roger, Small sample inference for fixed effects from restricted maximum likelihood. Biometrics 53, 983 (1997).

61. R. A. Friesner, J. L. Banks, R. B. Murphy, T. A. Halgren, J. J. Klicic, D. T. Mainz, M. P. Repasky, E. H. Knoll, M. Shelley, J. K. Perry, D. E. Shaw, P. Francis, P. S. Shenkin, Glide: A New Approach for Rapid, Accurate Docking and Scoring. 1. Method and Assessment of Docking Accuracy. J Med Chem 47, 1739–1749 (2004).

62. S. Jo, T. Kim, V. G. Iyer, W. Im, CHARMM-GUI: A web-based graphical user interface for CHARMM. J Comput Chem 29, 1859–1865 (2008).

63. N. Eswar, B. John, N. Mirkovic, A. Fiser, V. A. Ilyin, U. Pieper, A. C. Stuart, M. A. Marti-Renom, M. S. Madhusudhan, B. Yerkovich, A. Sali, Tools for comparative protein structure modeling and analysis. Nucleic Acids Res 31, 3375–3380 (2003).

64. K. Vanommeslaeghe, A. D. MacKerell, Automation of the CHARMM general force field (CGenFF) I: Bond perception and atom typing. J Chem Inf Model 52, 3144–3154 (2012).

65. G. A. Tribello, M. Bonomi, D. Branduardi, C. Camilloni, G. Bussi, PLUMED 2: New feathers for an old bird. Comput Phys Commun 185, 604–613 (2014).

66. G. Bussi, D. Donadio, M. Parrinello, Canonical sampling through velocity rescaling. Journal of Chemical Physics 126 (2007).

67. M. Bernetti, G. Bussi, Pressure control using stochastic cell rescaling. Journal of Chemical Physics 153 (2020).

68. T. Darden, D. York, L. Pedersen, Particle mesh Ewald: An N·log(N) method for Ewald sums in large systems. J Chem Phys 98, 10089–10092 (1993).

69. B. Hess, H. Bekker, H. J. C. Berendsen, J. G. E. M. Fraaije, LINCS: A linear constraint solver for molecular simulations. J Comput Chem 18, 1463–1472 (1997).

Figures

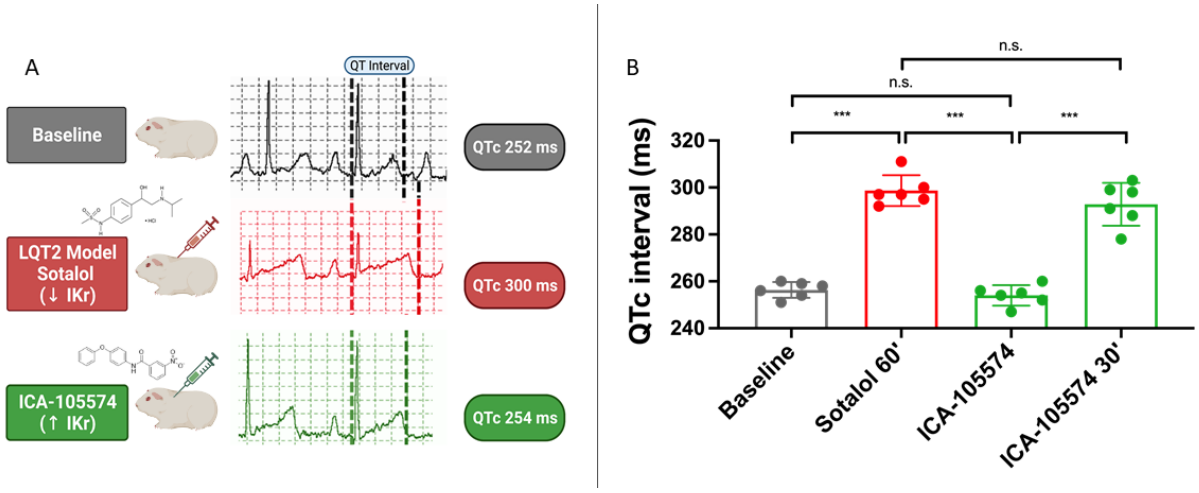

Figure 1. (A) *In vivo* LQT2 ECG recordings. LQTS was successfully induced in all animals after sotalol treatment (252±10 ms vs. 295±9 ms for the baseline and sotalol treated guinea pigs, respectively; $p<0.001$). Importantly, a pronounced and statistically significant shortening of the QTc interval was obtained in guinea pigs after ICA-105574 administration, normalizing the QTc in all animals (295±9 ms vs. 254±4 ms, before and after ICA administration, respectively). Importantly, despite the marked QTc shortening, no arrhythmic events were observed in the studied animals after ICA-105574 administration. (B) Pairwise comparisons were performed and the main relevant differences regarding the ECG values, are shown as histograms.

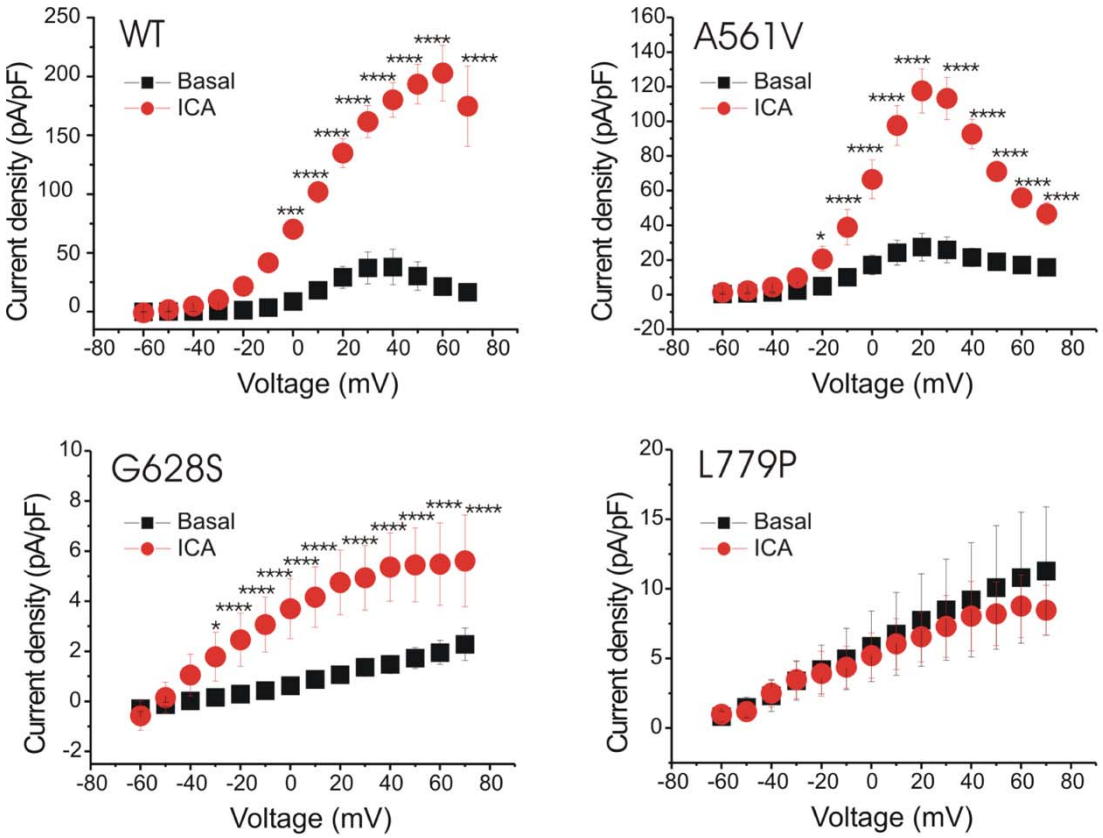

Figure 2. I/V relationships in hERG WT and mutants. The I/V graphs are derived by voltage clamp recordings showing WT, A561V, G628S and L779P activation currents recorded in basal condition (black square) and after 10 µM ICA-105574 perfusion (red dot). Each value is represented as mean□±□s.e.m. Statistical analyses were conducted using two-way ANOVA with Šidák post test. **P*□<□0.05, ***P*□<□0.01, ****P*□<□0.001 and *****P*□<□0.0001. WT: n=5, A561V: n=6, G628S: n=6, L779P: n=4.

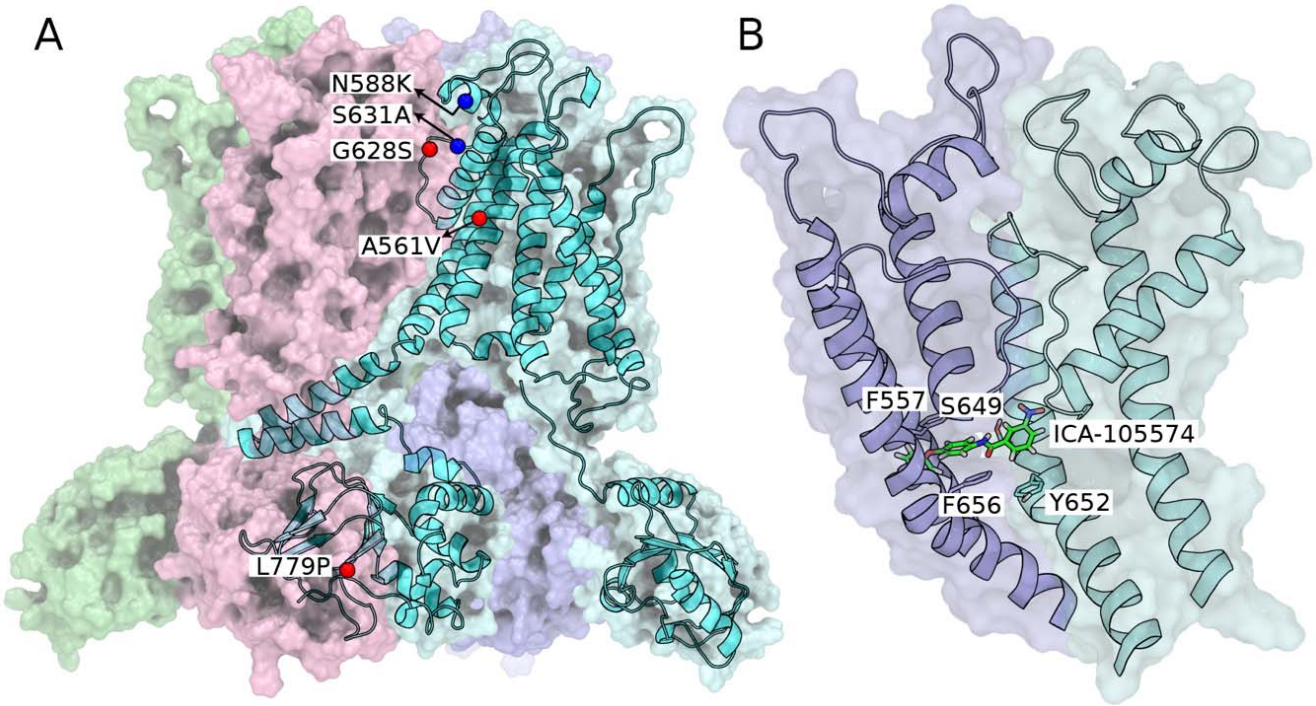

Figure 3. (A) Structural representation of the hERG tetramer with the SQT (N588K and S631A) and LQT (A561V, G628S and L779P) mutations highlighted in blue and red spheres respectively. A single monomer is shown with different domains identified in the cryo-EM structure (PDB: 5VA2). The SQT mutations, N588K and S631A, are located near the selectivity filter and are known to attenuate the inactivation state, whereas the LQT mutation G628S directly affects the selectivity filter. (B) ICA-105574 was docked into the hERG tetramer based on the previous mutagenesis study by Sanguinetti and co-workers (*28–30*). The docked structure is subjected to molecular dynamics (MD) simulations to obtain an equilibrated protein-ligand structure embedded in the lipid bilayer. The position of ICA-105574 in the equilibrated structure is consistent with previous findings and suggestions.

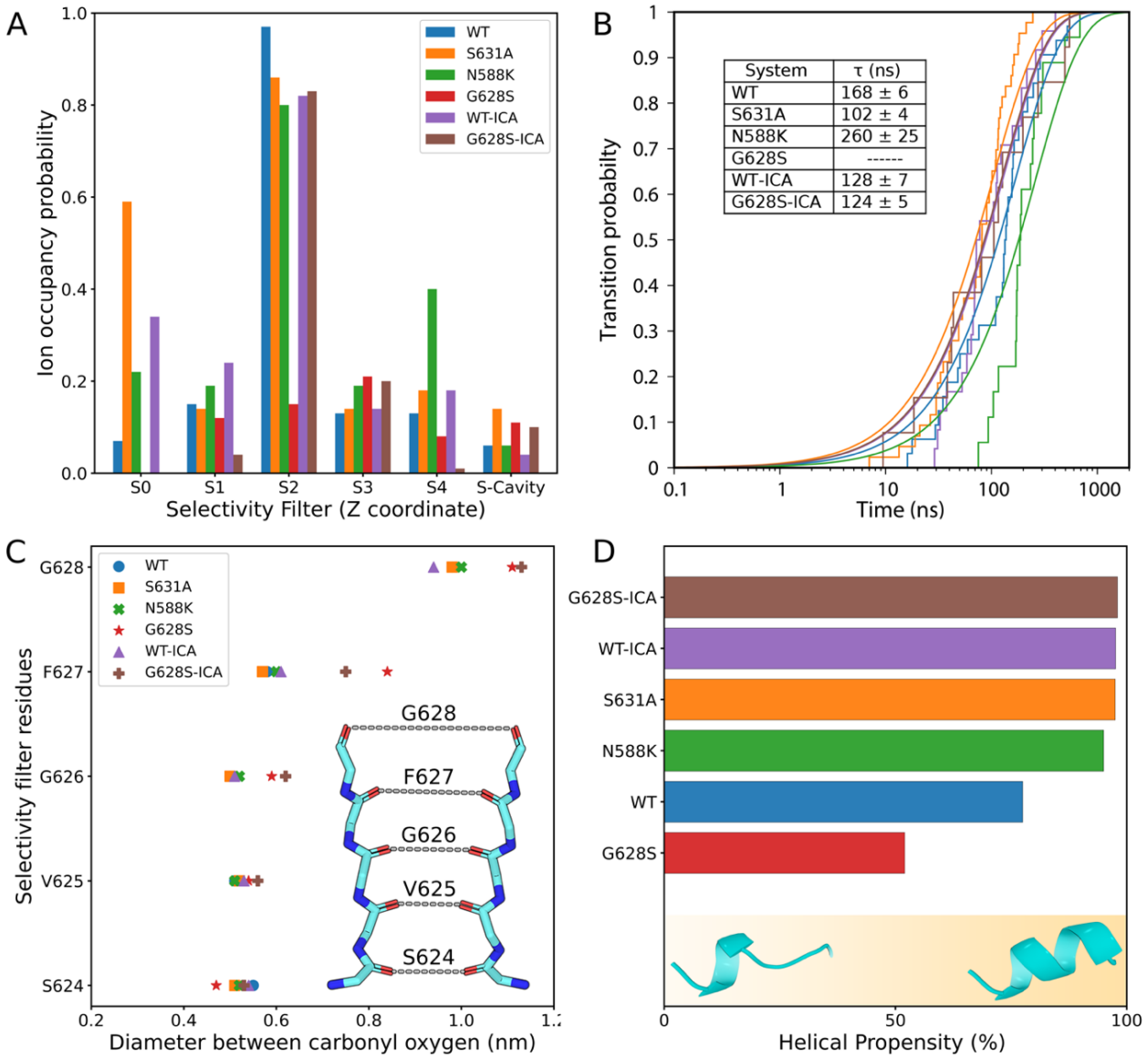

Figure 4. (A) The plot represents the ion occupancy probability at different sites in the selectivity filter over the simulations. The selectivity filter is divided into six different sites namely S0 to S4 and S-Cavity. (B) The plot describes the transition probability of an ion crossing event and the average transition time for a single permeation event. No new ion permeation event was observed for the LQT2-G628S system except for the ions initially placed to prevent SF collapse. The inset table shows the average transition time for an ion permeation event in the hERG channel. (C) Open state definition of SF: The plot shows the diameter of the SF averaged over all replica trajectories. The diameter is calculated by averaging over the interchain distance between the opposite carbonyl oxygens of the SF residues. The Mutation G628S increases the diameter of the SF at the extracellular side. (D) The plot shows the helical propensity (%) of the S5P turret helix (residue number 584 to 592) in different systems. The values were averaged over the monomers for the replicated trajectories. Two distinct population clusters were observed for the helical region. The lower helical propensity around 30% is a weakly ordered structure which is prominent in the G628S mutation, whereas the higher helical propensity (> 90%) is represented as a well-structured helix in WT, SQTs (N588K, S631A) and ICA-bound systems. For comparison, see in SI Appendix Figure S7, which shows the population density of helical propensity in different systems.

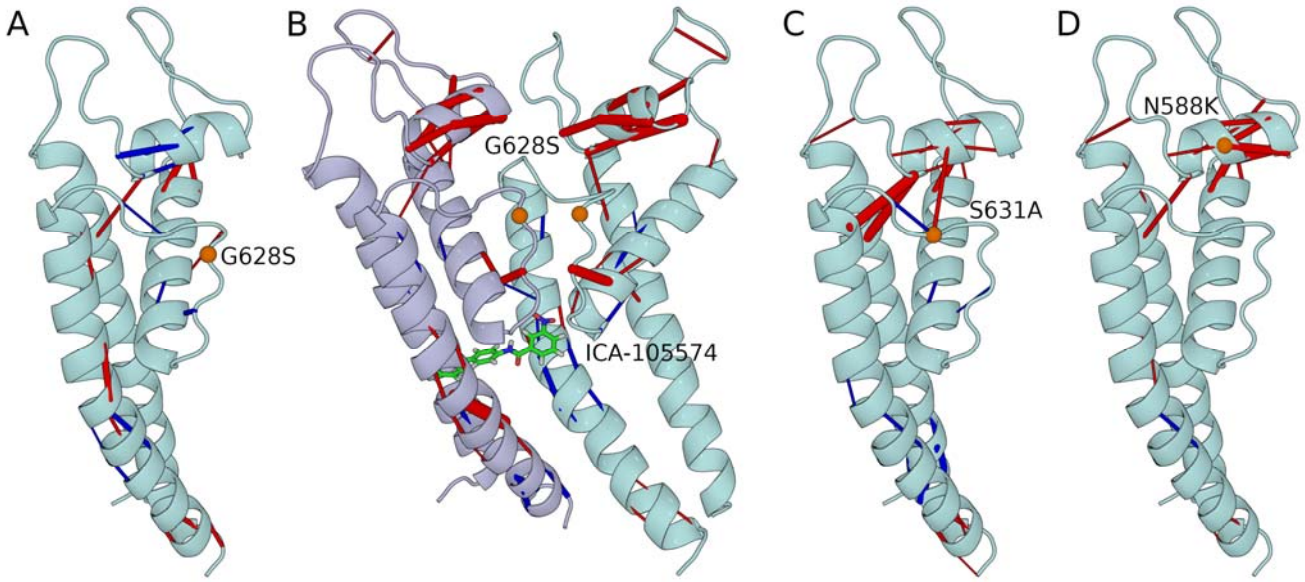

Figure 5. Hydrogen bond rearrangement upon perturbation in the form of mutations (G628S, S631A, N588K) or ligand binding (ICA-105574). The net H-bond occupancy (%) is highlighted in blue and red lines for the reference and the perturbed systems, respectively. The thickness of the lines represents the magnitude of the change. The mutations are shown as orange sphere. (A) Net H-bond occupancy (%) between G628S and WT ($\Delta HB_{ij} = HB_{ij}^{G628S} - HB_{ij}^{WT}$) shows the effect of the mutation in wild-type hERG: Blue lines show H-bonds that are lost in the mutant around the SF and the S5P turret helix, while red lines show H-bonds that are gained in the mutant at some residue pairs and the S6 helix end. (B) Net H-bond occupancy (%) between G628S-ICA and G628S ($\Delta HB_{ij} = HB_{ij}^{G628S-ICA} - HB_{ij}^{G628S}$) shows the rescue effect of ICA-105574: The figure shows two adjacent chains to represent different H-bonding patterns following the asymmetric binding of the activator in the hERG channel. ICA-105574 binding increases the H-bond occupancy around SF (Y616-S620, S620-G626) and S5P turret helix (G584-Q592) in both chains, while some residue pairs have opposite H-bond occupancy changes in G628S and ICA-105574 systems (e.g., E637-S641, M645-S649). (C, D) Net H-bond occupancy (%) between S631A and WT ($\Delta HB_{ij} = HB_{ij}^{S631A} - HB_{ij}^{WT}$), and between N588K and WT ($\Delta HB_{ij} = HB_{ij}^{N588K} - HB_{ij}^{WT}$) shows the effect of mutations in terms of gain in H-bonds in the mutants at S5P turret helix and some residue pairs around the S6 helix end.

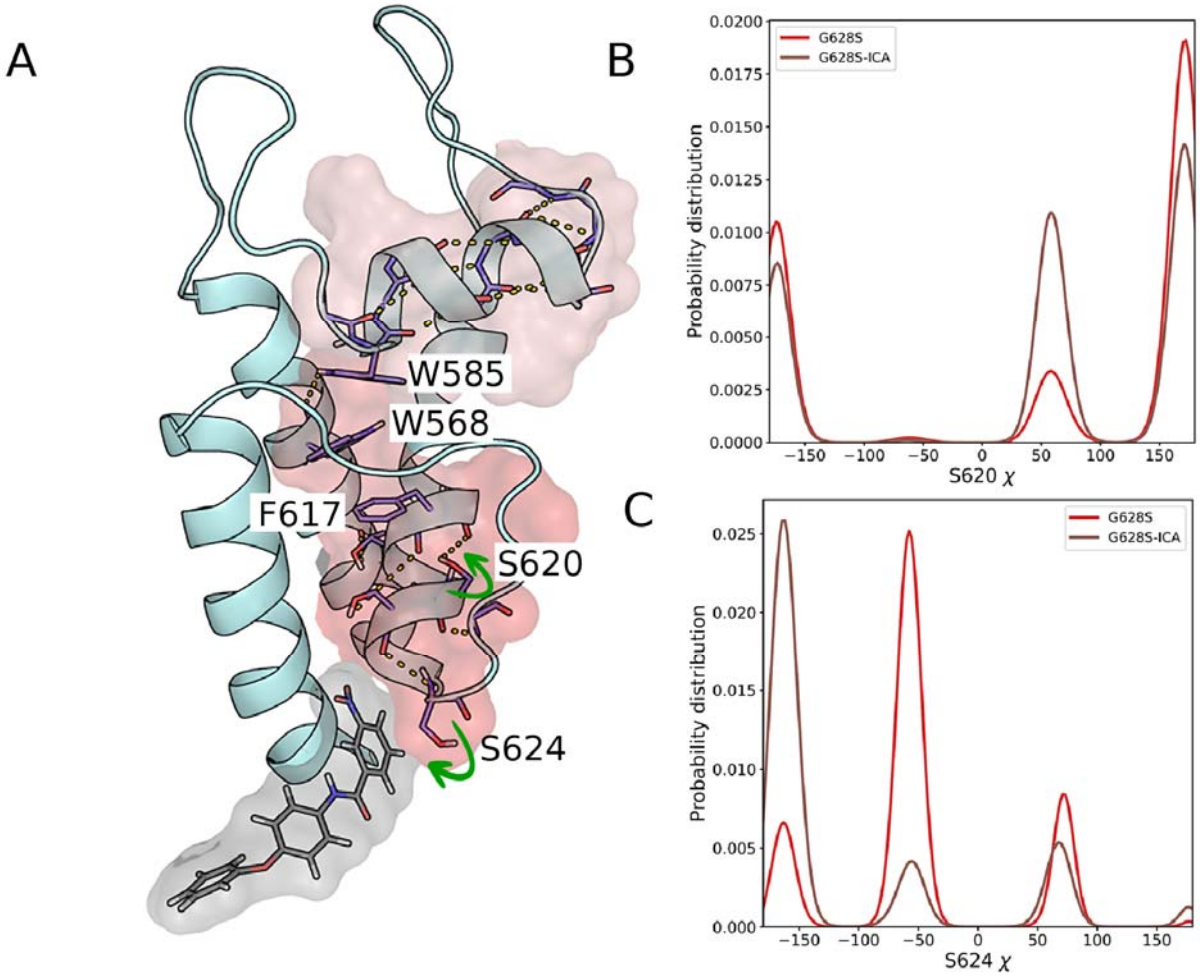

Figure 6. Mechanism of the rescue effect of the I_{Kr} activator ICA-105574 in the G628S mutation. (A) The figure shows a schematic representation of the allosteric network linking ICA-105574 binding to the SF and the S5P turret helix in a single monomer chain of the G628S mutant. ICA-105574 and the residues with higher net H-bond occupancy in the G628S-ICA system are highlighted as sticks, with H-bonds indicated by dashed lines. The surface representation shows the propagation path, with the gradual decrease in color indicating increasing distance from the ligand binding site. (B, C) S624 is defined as the starting point of the network because it forms a favorable interaction with the nitro group of ICA-105574. The Chi (χ)1 dihedral angle distributions of S620 and S624 are shown as 1D histograms, indicating significant population shifts or changes in the side chain orientations upon ICA-105574 binding.

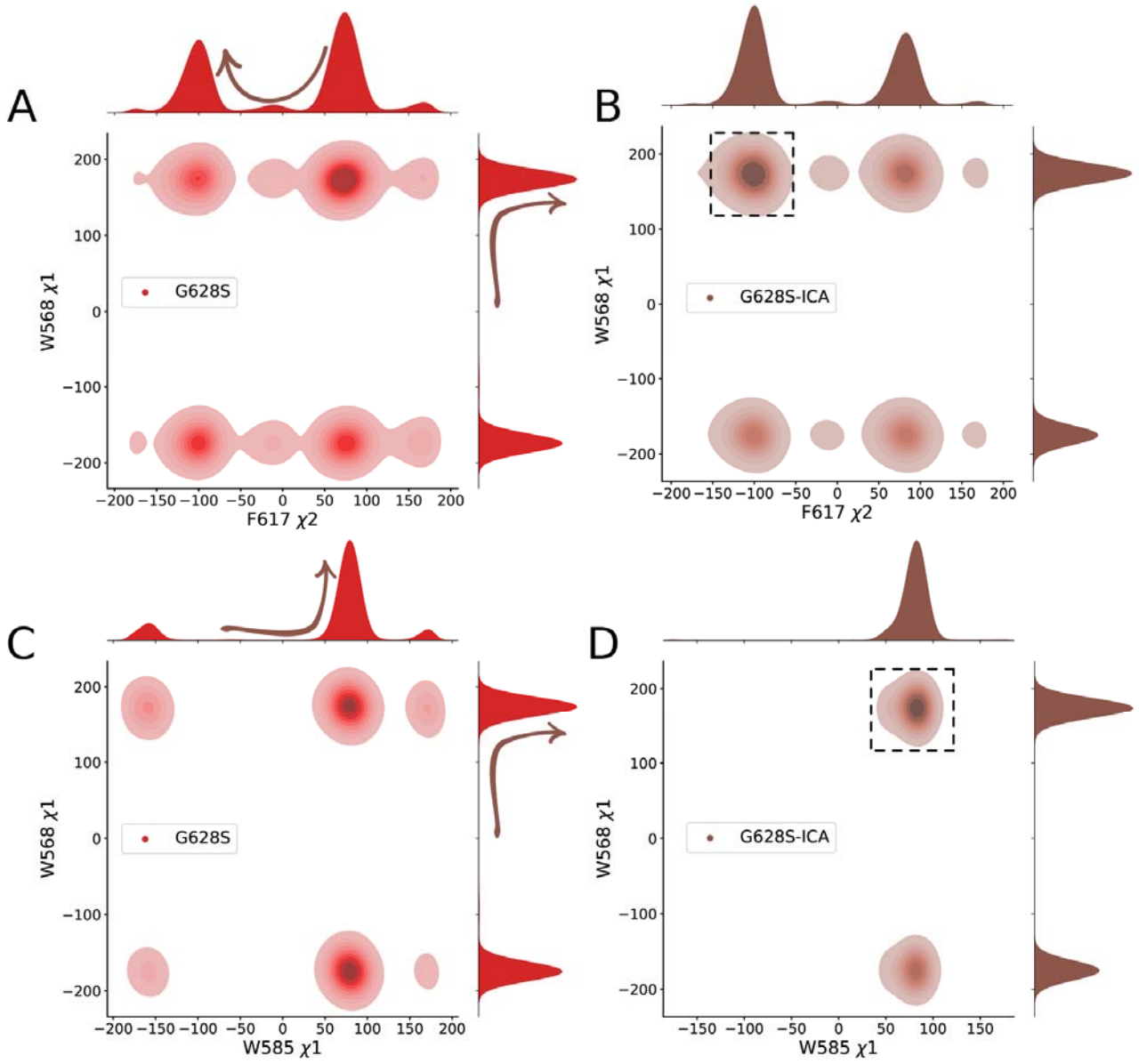

Figure 7. (A-D) χ2 dihedral distributions of residue pairs W568-F617 and W568-W585 in the G628S and G628S-ICA systems. The color opacity indicates the population density of each bin. The figure is plotted jointly for each axis variable with a 1D histogram to represent the population shift in the dihedrals. The arrows indicate the changes in the distribution upon ICA-105574 binding, while the dashed square box indicates the most populated basin in 2D distribution upon ICA-105574 binding. (A, B) show the 2D distribution of W568-χ1 and F617-χ2 angles, and (C, D) show the 2D distribution of χ1 angle for W585-W568.